

Structure of the subducting Nazca Plate beneath Peru

Edmundo O. Norabuena¹ and J. Arthur Snoke

Virginia Tech Seismological Observatory, Department of Geological Sciences, Virginia Polytechnic Institute and State University, Blacksburg

David E. James

Department of Terrestrial Magnetism, Carnegie Institution of Washington, Washington, D.C.

Abstract. Arrival times from intermediate-depth (110–150 km) earthquakes within the region of flat subduction beneath the subandean zone and foreland basins of east-central Peru provide constraints on the geometry and velocity structure of the subducting Nazca plate. Hypocentral locations and origin times for these events were determined using observations from a 15 station digitally recording locator array deployed in the epicentral region of eastern Peru. Observed *P* wave arrival times for coastal stations in Peru, some 3–6° from the epicenters, are up to 4 s early relative to predicted arrival times based on the best fit velocity-depth model used for hypocenter locations. These large negative time residuals appear to be the result of propagation paths which have long segments in the colder, higher-velocity subducting plate. *P* wave travel times were modeled for the effects of the slab using three-dimensional (3-D) ray tracing. Computed ray paths show that travel times to coastal stations for the eastern Peru events can be satisfactorily modeled with average velocities relative to the surrounding mantle 6% lower within the uppermost slab (assumed on the basis of other studies to be unconverted basaltic oceanic crust 6 km thick) and 8% higher within the cold uppermost mantle of the slab. Ray tracing for this plate model shows that *P* wave “shadow zones” can occur if the source-slab-receiver geometry results in seismic rays passing through regions in which the dip angle of the slab changes significantly. Such geometries exist for seismic waves propagating to some coastal stations from intermediate-depth earthquakes located east of the Andes. Observed first-arrival times for such cases do in fact have smaller negative residuals than those for geometries which allow for “direct” paths at similar distances. Modeling such arrivals as internally reflected waves propagating through the high-velocity part of the plate produces a significant improvement in the travel time residuals. For the slab velocities given above, we obtain a model thickness of approximately 36 km for the cold slab interior and a slight northwest component of dip in the region of subhorizontal subduction.

Introduction

The Andean margin between latitudes 0°S and 45°S can be subdivided into five tectonic segments that alternate between normal and flat subduction [e.g., *Stauder*, 1975; *Barazangi and Isacks*, 1976; *Jordan et al.*, 1983; *Cahill and Isacks*, 1992]. Zones of normal subduction are associated with active volcanism (Ecuador, southern Peru/northern Chile, and southern Chile (Figure 1)). Zones of flat subduction are characterized by the absence of volcanism (northern-central Peru and central Chile).

¹Now at Instituto Geofísico del Perú, Lima, Perú.

Copyright 1994 by the American Geophysical Union.

Paper number 94JB00126.
0148-0227/94/94JB-00126\$05.00

The present study focuses on the segment between 5° and 15°S latitude, considered the largest zone of flat subduction in the world. Here, the Nazca plate descends at about 30° dip until it reaches the approximate depth of 100 km, where it flattens and runs subhorizontally for several hundred kilometers before dipping steeply into the upper mantle [*Hasegawa and Sacks*, 1981]. The onset of horizontal subduction beneath central Peru appears to be related to a cessation of volcanic activity in the region [e.g., *Noble et al.*, 1974; *Barazangi and Isacks*, 1976; *Noble and McKee*, 1977]. Noble and McKee suggest on the basis of radiometric ages and field geology that Neogene volcanism along northern and central Peru ended gradually 5 Ma ago in the early Pliocene after a strong pulse of magmatic and volcanic activity (9.5 m.y.). Flat subduction and the absence of volcanism are apparently correlated with low heat flow measurements averaging about 30 mW/m² over the non-volcanic zones. In contrast, the heat flow val-

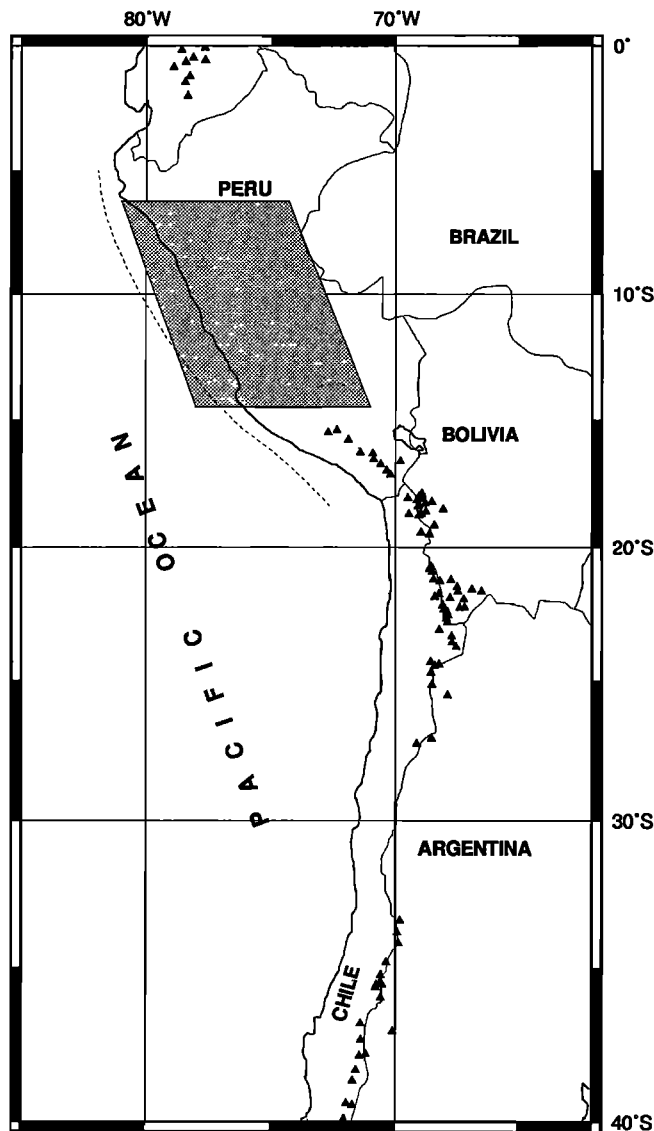


Figure 1. Map showing tectonic segmentation of Andean South America as delineated by the presence or absence of volcanoes (solid triangles). Regions of normal subduction (dip angle about 30°) are bounded by latitudes (0° – 2° S), (15° – 27° S), and (33° – 45° S). Regions in which there are no volcanoes correspond to the zones of flat subduction in northern-central Peru and central Chile. Area of study is indicated by shaded area. The Peru-Chile trench is shown by a dashed line.

ues measured above regions of normal subduction typically reach 60 mW/m^2 [Henry, 1981; Henry and Pollack, 1988]. As expected from the low heat flow, the crust and upper mantle in the zone of flat subduction beneath Peru are characterized by high Q ; values of Q_s have been found to be about 1000 within the slab and 500 within the overlying continental lithosphere [Sacks and Okada, 1974; Hasegawa and Sacks, 1981] (also J.F. Schneider and I.S. Sacks, Subduction of the Nazca plate beneath central Peru from local earthquakes, submitted to *Journal of Geophysical Research*, 1991; hereinafter referred to as submitted manuscript, 1991). The high

Q values apparently preclude the existence of asthenosphere between the slab and the overlying continental lithosphere.

In this paper we examine high-velocity propagation of longitudinal waves through the region of flat subduction beneath northern and central Peru (Figure 2). Analyses of travel times associated with these seismic waves are used to place constraints on the geometry of the slab and its velocity structure. To carry out the analysis, we selected intermediate-depth events (focal depths between 110 and 155 km) that occurred beneath eastern-central Peru, and which were well recorded by the two networks shown in Figure 2: a local network of portable digital recorders and a permanent telemetered set of stations located along the Peruvian coast. The local network, deployed for a period of several weeks in the epicentral region, served as a locator array. Travel times to the telemetered network (not used in hypocenter determination) were used to constrain the structure of the subducting plate.

High-quality hypocentral determinations for the events used in this study were obtained using the locator array and a regional one-dimensional (1-D) velocity structure. Large travel time residuals for first arrivals at coastal stations for these events were systematically negative for the 1-D model, suggesting that the propagation paths were through the high-velocity interior of the slab. As shown below, 3-D ray tracing through a slightly modified version of the Hasegawa and Sacks

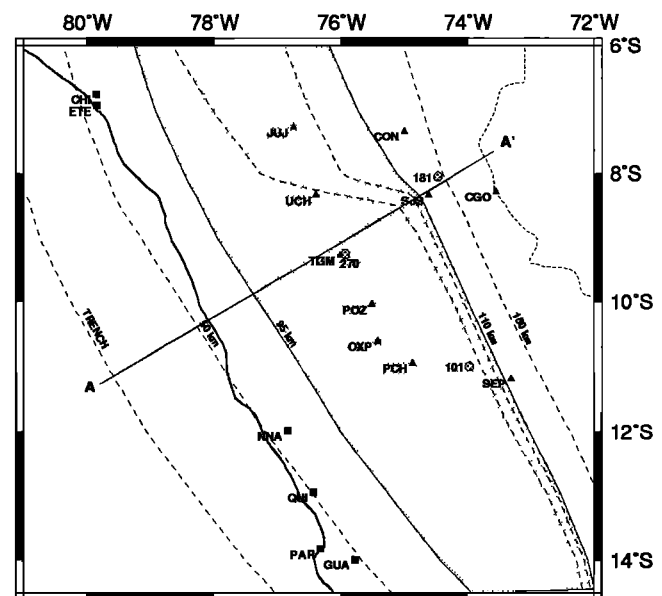


Figure 2. Distribution of seismic stations for the PE85 experiment. Coastal network stations are represented by solid squares and stations of the locator network by solid triangles. Epicenters for the three events used in this study are shown as stippled circles. Dashed lines represent isodepth contours of the Nazca plate at the trench and at depths of 50, 95, 100, 105, 110, and 150 km. The shaded region, delimited by contours at depths of 95 and 110 km, is the region of subhorizontal subduction. Line A–A' denotes cross section shown in Figure 3.

[1981] slab model (Figure 3) produces consistent results if the average velocity and thickness of the slab interior are chosen appropriately.

Data

The earthquakes used in this study are from the data set obtained in 1985 during an experiment carried out by the Department of Terrestrial Magnetism (DTM/CIW) and the Instituto Geofísico del Perú (IGP) over the subandean and eastern Peru basin provinces of central and eastern Peru (J.F. Schneider and I.S. Sacks, submitted manuscript, 1991). A description of the seismic networks and our processing procedures follows.

Seismic Networks

The local network consisted of 14 portable digital seismographs composed mainly of University of Wisconsin three-component digital recorders (UWR) with 1-Hz geophones. Station locations are shown as solid triangles in Figure 2. Absolute Omega timing accuracy of the Wisconsin instruments is better than 0.01 s.

The coastal network consisted of five 1-Hz permanently installed telemetered stations, CHI, ETE, QUI, PAR, and GUA, and the (analog) World-Wide Standard Seismograph Network (WWSSN) station at NNA. Only stations NNA and GUA are three component, the others are vertical only. The data from the telemetered stations were recorded digitally at a central recording site. Phase arrival times for stations ETE and CHI, event 181, and NNA, event 101, were obtained from the IGP seismic bulletins. Timing is via a GOES satellite clock and is considered accurate at the millisecond level.

The local network was operational for approximately 3 months, during which time a total of 512 (mostly unlocated) events were recorded, including 80 intermediate focal depth earthquakes (the PE85 data set) located

within the subducting slab beneath the array. Although 25 of these events were also recorded to varying degrees by the coastal array, only events E101, E181, and E270 had hypocenters located within the local network and clear *P* arrivals on at least four coastal stations.

Data Processing

For the eastern portable network, *P* wave arrivals were read from the unfiltered vertical component seismograms while *S* wave arrivals were read from the horizontal components. The records typically exhibit simple waveforms, one example of which is shown for event E270 in Figure 4.

Seismograms recorded at the coastal stations exhibit far greater complexity than do those of the portable network (e.g., Figure 5). To eliminate very high frequency noise, the seismograms were low-pass filtered using a four-pole Butterworth filter with an 8-Hz corner frequency.

Hypocenter Locations

Earthquakes in eastern Peru were located using observations from only the portable array. The accuracy of these locations is critical for the present study, which is based on travel time residuals of *P* waves traveling regional distances to coastal stations. The constraints imposed by observed travel time anomalies on the geometry and velocity structure of the subducting Nazca plate are significant only to the extent that the locations and origin times of the events are accurately known.

Early studies of the seismicity and, inferentially, of the geometry of the Nazca plate beneath central and eastern Peru were based on teleseismic data [e.g., Barazangi and Isacks, 1976]. More recent studies by Hasegawa and Sacks [1981], Boyd *et al.* [1984], and

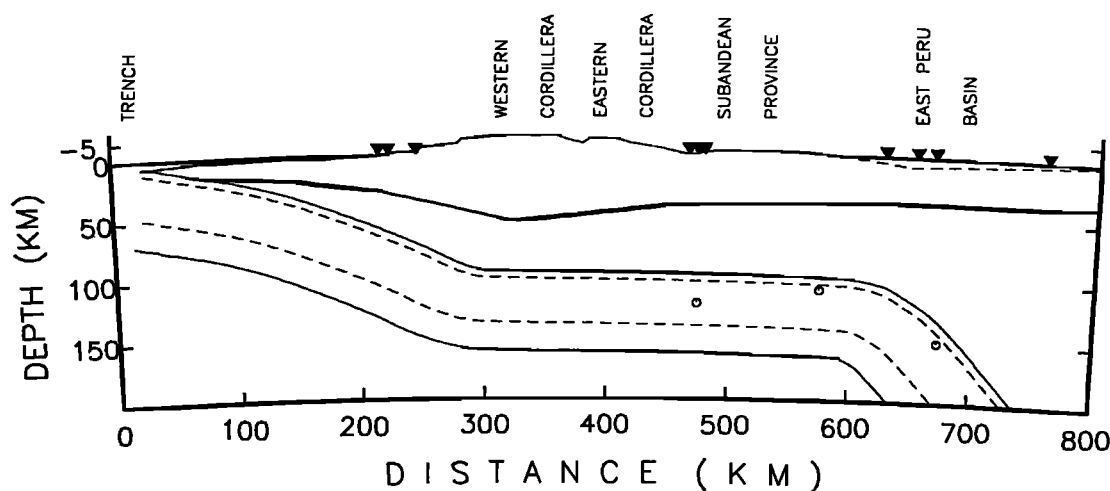


Figure 3. Structure of the Nazca plate subducting beneath central Peru. Slab model is comprised of three layers: a 6-km-thick upper layer of unconverted basaltic crust, a high-velocity peridotitic interior layer ≈ 36 km thick, and a lower transitional region ≈ 23 km thick. The 800-km cross section has an origin at 11.25°S and 79.8°W and an azimuth of 62° . Open circles denote the three hypocenters used in this study. The inverted solid triangles are projections of the seismic stations onto this section.

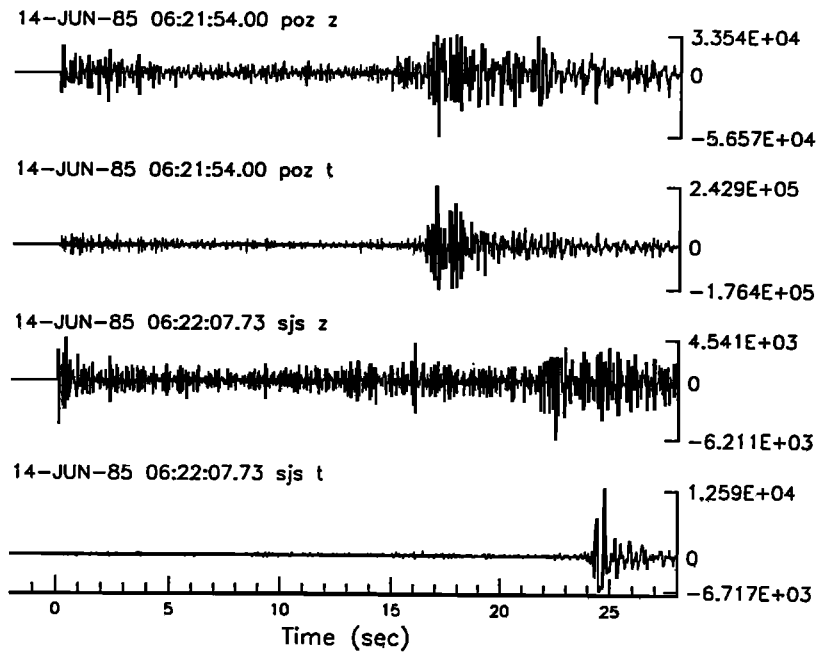


Figure 4. Vertical and transverse component seismograms for event E270 recorded at stations POZ and SJS in the locator network.

Schneider and Sacks [1987] were based on data from a local seismic network in southern Peru, for which about 2000 well-determined locations were obtained. These locations served as the primary data for deriving the Hasegawa-Sacks model for the upper boundary of the subducting Nazca plate in this region.

It was not until the PE85 experiment that high-quality recordings of earthquakes beneath central-

eastern Peru were obtained. The locator array was deployed in the region directly above the flat segment of the slab and the region of resubduction (where the slab again dips steeply into the mantle). The location of the network is such that the take-off angles for rays from the intermediate-depth earthquakes are nearly vertical. Accordingly, slab effects on travel times are negligible (e.g., see Figure 3).

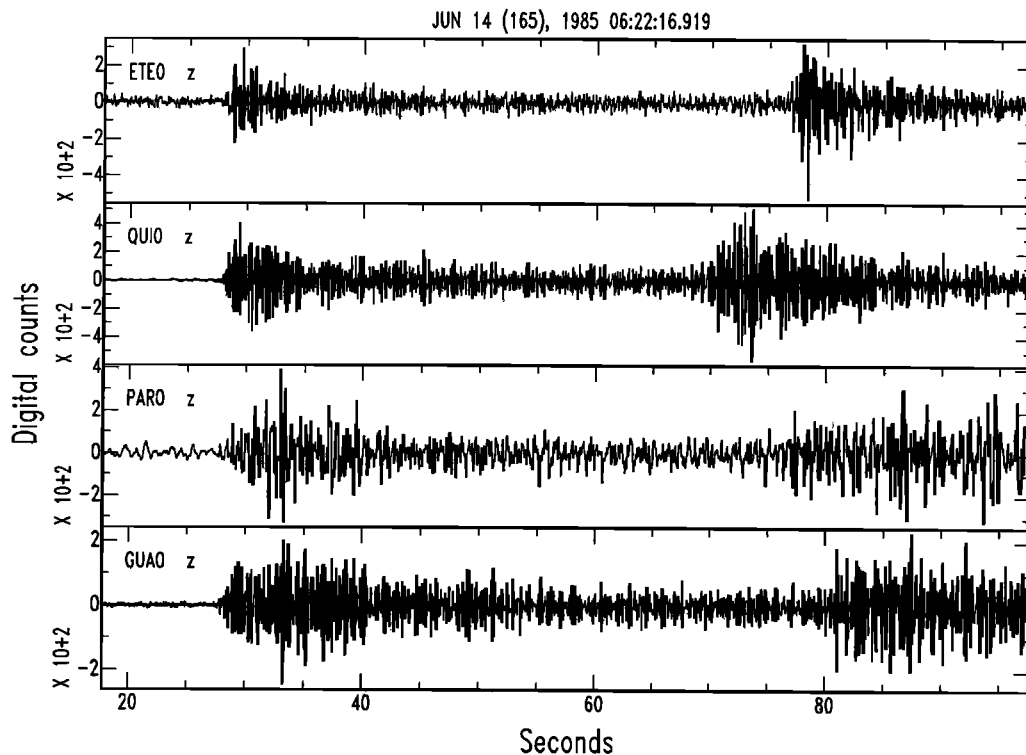


Figure 5. Vertical component seismograms from coastal stations for event E270. Traces have been low-pass filtered with a corner at 8 Hz.

Location Procedure and the 1-D Velocity Structure

The starting velocity structure for the crust and upper mantle beneath central-eastern Peru was derived from surface wave studies over central Peru, Bolivia, and northern Chile [James, 1971]. V_P/V_S ratios were varied assuming that crystalline crustal rocks have a Poisson's ratio of about 0.26 and mantle rocks have higher values which increase with depth. The effect of sedimentary layers underlying stations in the Ucayali Basin, as determined by James and Snoke [1994], were included as station delays.

Travel time computations were based on a spherical Earth model. Travel time tables for P and S waves were generated for the selected velocity model using the IASPEI91 procedure [Kennett and Engdahl, 1991] modified to handle a tabular model input. The tables based on wave propagation through a spherically symmetric Earth model were used with Hypoellipse [Lahr, 1992] (which includes extensions by Snoke and Lahr to utilize such tables) to determine locations. P and S arrival times were used for all locations. Only those arrivals recorded on the locator array were given nonzero weight.

The 12 intermediate-focal-depth earthquakes best recorded by the stations making up the locator array were used to fine tune the velocity model. The selection criteria for the best model were based on average root-mean-square residuals (rms) and the Hypoellipse quality classification scheme.

The derived velocity model, given in Table 1 and termed VMP85 (Velocity Model Peru 85), produced the smallest residuals for the 12 test events: an average rms residual of 0.29 s, with 70% of the events rated as quality B, and 23% rated C.

Table 2 gives the hypocentral location and origin time for the three events used in this study. The estimated uncertainties in distance and depth at the $\pm 1\sigma$ level were less than 3 km. Origin time standard errors were less than 0.4 s.

Travel Time Analysis to Coastal Stations

Table 3 includes P wave travel time residuals to coastal stations obtained with the 1-D VMP85 velocity model. Residuals (observed - calculated) are systematically negative, indicating that compressional wave propagation to coastal stations is faster than predicted.

Table 1. Model VMP85: Velocity Structure Beneath Central Peru

Depth, km	V_P , km/s	V_P/V_S
00.00	6.00	1.76
20.00	6.00	1.76
20.00	6.50	1.76
35.00	6.50	1.76
35.00	7.95	1.77
85.00	8.00	1.77
125.00	8.05	1.78
165.00	8.15	1.79

The residuals typically become more negative as epicentral distance increases, although the northernmost stations CHI and ETE consistently exhibit larger residuals (about -4 s). No station corrections except for elevation are considered, but we estimate these to be at most a few tenths of a second.

The travel time residuals are far too large to be attributed solely to inaccurate locations or origin times. Typical error estimates for origin time, for example, are around ± 0.3 s. Moreover, in trial solutions based on a wide range of 1-D velocity models, we could find no 1-D model which would produce an overall reduction in the travel time residuals.

Subducting Plate Structure and 3-D Ray Tracing

Plate Structure

The most plausible explanation for the residuals, and the one which we propose here, is the influence on travel times of the high-velocity slab. In this section we review the constraints on the structure of the subducting plate based on 3-D ray tracing through the slab.

Based on the earlier seismicity studies, the oceanic slab descends beneath northern-central Peru at an angle of 30° to an approximate depth of 100 km, where it flattens and runs subhorizontally for a distance of 300–400 km before resubducting steeply into the upper mantle. The upper boundary of the subducting Nazca plate used in this study is based on models obtained from studies of local seismicity and converted phases in central-southern Peru, chiefly Hasegawa and Sacks [1981], but also Boyd *et al.* [1984] and Schneider and Sacks [1987]. Figure 2 shows isodepth contours (dashed lines) to the top of the slab for our preferred slab model, which is a slight modification of the Hasegawa-Sacks model. Hasegawa and Sacks [1981] estimate that depth resolution for the top boundary of the subducting plate in the flat-subduction region is about 10–15 km, and the uncertainty in the distance from the trench for the onset of resubduction is about 20 km.

Sacks [1983] examined the question of flat subduction and slab buoyancy in considerable detail for central Peru. He observed that the low regional heat flow (about 30 mW/m²) in central Peru combined with the young age of subducted oceanic plate (≈ 50 Ma) and its high rate of subduction (about 10 cm/yr), all act to retard the basalt-eclogite transformation in the descending oceanic crust. Sacks showed that when the basalt-eclogite transformation is delayed, the plate can remain buoyant for long periods of time. Retardation of the basalt-eclogite transition is known to occur when slab temperatures fall below about 600°C [e.g., Ahrens and Schubert, 1975; Fukao *et al.*, 1983]. Thus for modeling purposes, we assume that flat subduction is the result of slab buoyancy, with the basaltic crust of the descending slab assumed to have a density of about 2.8–2.9 Mg/m³. The P wave velocity in the basaltic crust at a depth of 100 km is estimated from the work of Matsuzawa *et al.* [1986, 1987] to be about 6% below that

Table 2. Hypocentral Locations for Events E101, E270, and E181

Event	Date in 1985	Julian Day	Origin time	Latitude, deg S	Longitude, deg W	Depth, km	rms
101	June 1	152	0435:55.9	10.95	73.97	110	0.25
181	June 7	158	1125:05.0	8.04	74.48	152	0.38
270	June 14	165	0621:42.6	9.24	75.94	121	0.29

of the surrounding mantle. The choice of thickness and velocity contrast of the crustal layer in the slab has only a second-order effect on the modeling results presented below.

For the very low heat flow observed in central Peru (about 30 mW/m²), estimated temperatures in the continental lithosphere at 100-km depth will be unusually low, about 400–500°C [Chapman and Pollack, 1977]. Estimates of the interior temperatures in the subducting slab are more difficult and are quite model dependent. The slab beneath central Peru is estimated to have an age of about 50 Ma and a total thickness of 60–70 km [Sacks, 1983]. Because of the very low temperature of the overthrust continental lithosphere in the zone of flat subduction, we take the internal thermal structure of the slab to be similar to that in the slab before subduction. Based on that assumption, temperatures in the slab should be about 350°C at a depth of 15–20 km inside the slab and approximately 600°C at a depth of 30–35 km [e.g., Watts et al., 1980; McNutt, 1984]. As we shall show below, even these relatively low temperatures may be somewhat too high to explain the very high slab velocities observed.

In the 3-D ray tracing calculations discussed below, the cold ultramafic interior of the slab is modeled as a

single constant thickness layer sandwiched between the overlying (low velocity) oceanic crust and a transitional zone in the lower slab gradational with the underlying asthenosphere. The aim of the present study is to provide constraints on the average velocity and thickness of the lower-temperature high-velocity zone in the interior of the slab.

3-D Ray Tracing

Several numerical methods have been developed to study the wave propagation within laterally heterogeneous mediums using ray theory [e.g., Jacob, 1970; Julian, 1970; Červený et al., 1988; Vidale, 1990]. The method described here is based in part on Jacob's numerical approximation to the ray equations and follows the initial value approach (shooting method) as opposed to the boundary value approach (bending method) [Julian and Gubbins, 1977].

We make use of the fact that the subducting plate strikes approximately north-south to tabulate data that define the upper boundary of the slab, as longitude values corresponding to increments of 1° in latitude per 5-km depth. Intermediate points are obtained using a cubic-spline interpolation procedure with no overshoot [Wiggins, 1976]. The boundaries of the intermediate

Table 3. Travel Time Residuals Associated With the 1-D and 3-D Velocity-Depth Models

Event	Station Code	Δ , km	Azimuth, deg	t_{obs} , s	δt_{1-D} , s	δt_{3-D} , s
101	NNA	333	250	46.5	0.4	1.1
101	QUI	347	230	46.8	−0.9	0.1
101	GUA	389	210	51.5	−1.3	−0.3
101	PAR	408	219	53.2	−1.8	−0.6
181	NNA	508	210	67.9	0.0	(0.6)
181	QUI	583	201	75.5	−1.3	(0.1)
181	ETE	606	281	75.3	−4.2	−0.8
181	CHI	611	283	76.0	−4.1	−0.7
181	PAR	672	197	85.7	−1.7	((0.1))
181	GUA	674	192	86.6	−1.1	((−1.1))
270	NNA	319	198	44.0	−0.8	0.1
270	QUI	413	187	53.4	−2.5	−1.1
270	ETE	501	300	62.0	−4.4	−2.2
270	PAR	509	185	64.9	−2.6	(−0.1)
270	CHI	512	302	64.6	−3.2	−0.9
270	GUA	527	178	66.6	−3.0	(−1.0)

Festooning 3-D ray path residuals are in parentheses. "Double bounce" ray paths have double parentheses.

and bottom layers are obtained by projections of the upper boundary surface for fixed latitude and depth so as to preserve constant layer thicknesses. The velocity contrasts and the thicknesses of the layers are input variables to the model.

The slab layers are modeled as laterally homogeneous. Following Jacob's approach, ray paths in the slab are created by extrapolation with a small step size, in our case 1 km. When a ray path encounters a slab boundary, the seismic ray is projected onto that boundary and Snell's law is applied to calculate the azimuth and takeoff angle of the outgoing ray. The program can handle transmission, conversions, and reflections at each boundary. In the present case there are no conversions, but we do make use of reflections to simulate a "festooning" mode (see next section).

An iterative process similar to the shooting method described by *Julian and Gubbins* [1977] is used to illuminate the coastal stations with a bidimensional fan of rays which take off from a grid of angles and azimuths expanded about the pair (azimuth, takeoff angle) obtained with the 1-D modeling. The grid of surface arrivals obtained in this way is compared with the station location, and the pair (azimuth, takeoff angle) of the closest ray is taken as the center of a new grid. The process is repeated until a ray arrives within 250 m of the station.

The slab model includes an uppermost layer (unconverted basaltic oceanic crust) with an assumed thickness of 6 km. The velocity contrast between that layer and the surrounding mantle is taken to be -6% based on values for subducted oceanic crust [*Fukao et al.*, 1983; *Matsuzawa et al.*, 1986]. The cold ultramafic layer beneath the oceanic crust is modeled for different thicknesses and velocity contrasts to obtain a best fit to the observed data. The layer thickness was varied between 30 and 50 km, and velocity contrast with surrounding mantle was varied between 5 and 10%.

Station PAR is closest to the trench of all the stations and is only about 25 km above the top of the subducting plate. To assure that ray paths to PAR had Moho conversions outside the slab, we changed the Moho depth to 30 km in our reference velocity model for both 1-D and 3-D paths to PAR.

Shadow Zones

Three-dimensional ray tracing shows that the contortion introduced in the slab when the dip changes rapidly can produce *P* wave "shadow" zones where no direct ray path through the slab exists for certain event/station pairs. In such a case, ray paths leading to first arrivals involve scattering and/or reflections caused by velocity heterogeneities within the subducting plate. We simulate a subset of such ray paths, referred to henceforth as "festooning" rays, by allowing reflections from the bottom and top of the cold slab interior. We find that it is possible to get several arrivals within a few tenths of a second for such festooning rays, a result consistent with the emergent and complex first arrivals seen for these event-station pairs. (Festooning rays commonly

exist for geometries for which a direct ray is possible, but because the festooning rays have a longer ray path, they will arrive after the direct arrival.)

3-D Ray Tracing Results

The slab model which evolves from arrival time residual reduction based on 3-D ray tracing is a slightly modified version of the original Hasegawa and Sacks model. In that model the depth to the upper slab boundary in the region of subhorizontal subduction is a constant ≈ 100 km for all latitudes, and the combined thickness of the upper two layers is ≈ 50 km. As discussed above, all our models assume a 6-km-thick upper layer with a velocity contrast of -6%, a feature not included in the original Hasegawa and Sacks model.

Results for each of the three events studied are presented in the discussion that follows.

E101

Figure 6 is a map view of surface crossings of direct rays starting from the hypocenter for E101 and traced through the plate model. Equal steps in takeoff angle and in takeoff azimuth were used, with limits chosen so that rays to all coastal stations were included. It is clear from this figure that all stations can be reached by direct rays and that there are no severe focusing or defocusing effects. Figure 7 shows the direct-ray propagation path in a cross section obtained by projecting the slab and ray trajectory onto a great circle path between the epicenter and station GUA.

Arrivals which correspond to direct-ray paths constrain the velocity contrast within the high-velocity layer. Assuming that contrast to be a constant, we get the maximum variance reduction for a contrast of 8%.

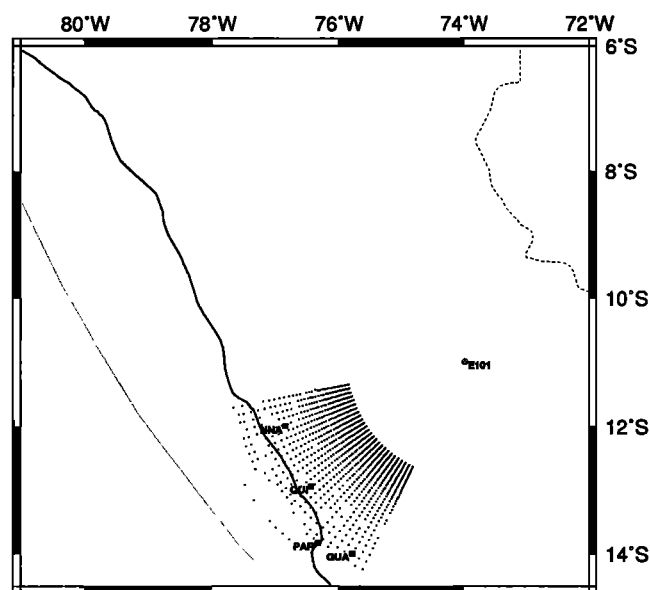


Figure 6. Map of surface intersections (small dots) of direct rays for event E101 traced through the 3-D slab model for equal increments of azimuth and take-off angle.

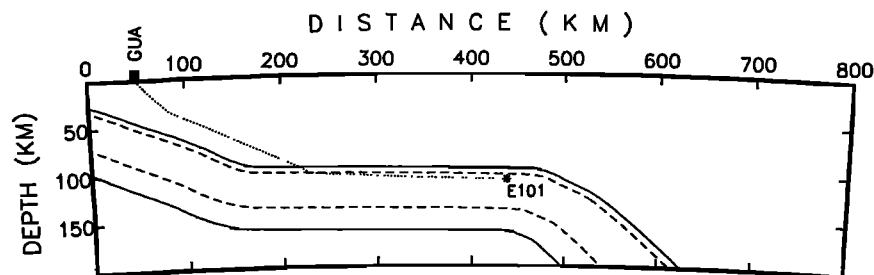


Figure 7. Direct-arrival ray path to station GUA from E101 traced through the 3-D slab model. The projection is through the station and along azimuth 30° .

As shown in Table 3, the travel time residuals to coastal stations GUA, PAR, and QUI are reduced substantially for the 3-D model compared to the 1-D model. The exception is the residual for NNA for which the 3-D models produce a larger residual: 1.3 compared to 0.5 s. We consider NNA for E101 to be anomalous, given that the 1-D residual at NNA for E101 is positive. (As noted above, NNA for E101 is the only case for which we had to rely on catalog readings of an analog record, rather than on our own reading of the seismogram. Based on other cases for which we had both catalog and direct readings, we anticipate this would make no more than a couple of tenths of a second difference.)

E181

E181 is the deepest of our events (≈ 150 km) and is at the greatest epicentral distance from coastal stations. The northernmost stations CHI and ETE have substantially more negative residuals than do the more southern stations PAR and GUA even though those stations have greater epicentral distances (Table 3). Assuming a constant velocity contrast, the pattern of residuals suggests direct slab propagation paths for the northern stations CHI and ETE, and festooning-mode propagation for the southern stations PAR and GUA. The differing kinds of propagation required to satisfy the observed arrival times at the coastal stations place constraints on both the thickness of the cold interior layer and the morphology of the upper slab boundary in the subhorizontal zone.

Figure 8 is a map view plot for surface crossings of direct rays starting from the E181 hypocenter and traced through the 3-D model. In this figure, the long-distance cutoff represents the physical boundary of a shadow zone. Note that direct rays can get to CHI and ETE, but no direct rays (see Figure 9) can get to any of the stations of the southern group of coastal stations (NNA, QUI, GUA, and PAR). In fact, modeling of ray paths to stations GUA and PAR produces the interesting result that those stations can be reached only by double-bounce festooning rays as shown in Figure 10 and indicated in Table 3 by a double set of parentheses.

Figure 9 shows why there is a shadow zone at NNA for E181. The (dotted line) ray path which intersects the lower boundary at about 140-km depth and refracts out of the bottom of the slab would have reached NNA if the thickness of the high-velocity layer in the slab were

increased by a few kilometers. The ray path indicated by a long-dashed line in Figure 9 shows a festooning ray from E181 to NNA. Times for such single-bounce, festooning ray paths are indicated with a single set of parentheses in Table 3.

Similar results to those for NNA are found for station QUI from E181. The fact that no direct rays reach either of these southern stations places tight modeling constraints on the thickness of the high-velocity layer for a given velocity contrast in the slab. Velocity contrast and thickness of the high-velocity layer are highly interdependent, but for a velocity contrast of 8% in the slab the calculated thickness of the high-velocity layer necessary to fit the observed travel times is 36 km, which is 8 km thinner than for the Hasegawa-Sacks slab model.

Reducing the thickness of the high-velocity layer to 36 km creates a problem with preserving direct paths to ETE and CHI, where travel time residuals demand very high-velocity propagation. To resolve this difficulty, we

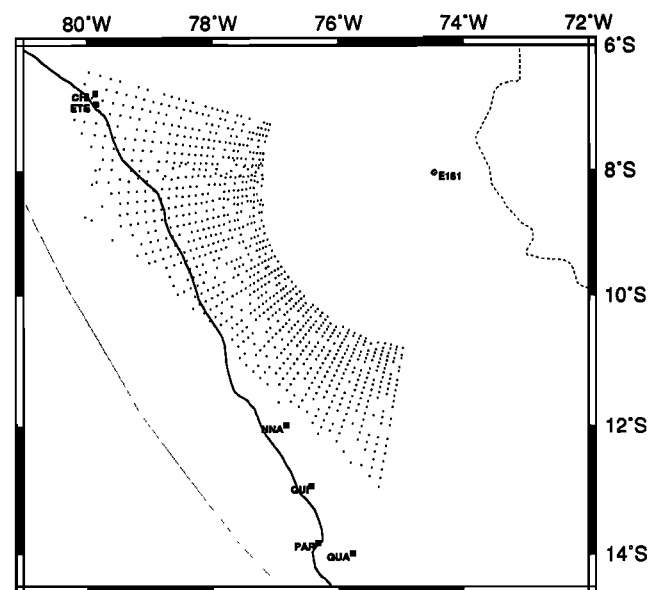


Figure 8. Map of surface intersections (small dots) of direct rays from event E181 traced through the slab model in equal increments of azimuth and takeoff angle. Note that stations NNA, QUI, PAR, and GUA are in a shadow zone for direct rays through the slab.

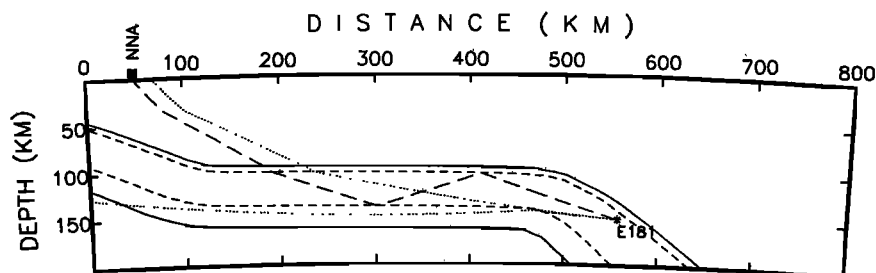


Figure 9. Ray paths to station NNA from E181 traced through the slab model. Dotted lines are for direct ray paths, none of which reach the NNA, which is in a shadow zone for direct *P*. The ray path shown by long dashes is a doubly reflected "festooning" ray, which is the probable first arrival at the station. The projection is through the station and along azimuth 30° .

modified the geometry of the upper plate boundary so that it included a slight component of dip to the NNW. This modification to slab morphology adopted for the purposes of ray path modeling is also consistent with the hypocentral location data which suggest that the upper boundary of the subhorizontal segment of the plate dips to the NNW and is 5–10 km deeper north of about 8°N latitude [I.S. Sacks, personal communication, 1993]. Evidence for this is also seen from the locations of all events recorded during the 1985 experiment, which indicate greater focal depths to the NNW.

E270

Figure 11 is the map view of direct-ray surface crossings from E270. Stations QUI, NNA, CHI, and ETE are all reachable by direct rays, and the 3-D residuals are all substantially less than the 1-D residuals (Table 3).

PAR and GUA cannot be reached by direct rays, but for a different reason than that discussed for ray paths from E181. Figure 12 shows why a shadow zone exists: the great circle path is along the azimuth for PAR, but no direct ray can get there because of the geometry of the plate's upper boundary: rays traveling towards PAR intersect the slab upper boundary in a region where that boundary changes slope abruptly. (Note in Figure 5 the emergent and complex first arrivals seen at PAR and GUA compared to those at ETE and QUI.) Modeling these two arrivals as single-bounce festooning rays produces a substantial reduction in the residuals.

Summary and Conclusions

An objective measure of the improvement in the travel time residuals of the 3-D model compared to the 1-D model is the percent reduction in the variance of the residuals. If we include the residual for E101 at NNA, the reduction is 71%. If we omit the residual for E101 at NNA, the variance reduction is 73%.

We conclude on the basis of the travel time residuals and the relative complexity of the *P* wave codas that arrivals at NNA and QUI for event 181 are better modeled as festooning rays than as direct rays. If correct, this observation places definite constraints on the slab model. The model is constructed to preserve all other direct (high-velocity) ray paths required by the travel time observations, particularly those for stations CHI and ETE. The model is, of course, nonunique in that there are inevitable trade-offs in slab shape, thickness, and velocity, as well, of course, in other lateral variations in the velocity structure of the slab and surrounding mantle. Thus, given the assumptions of our model calculations, the thickness of the high-velocity layer is determined to the nearest kilometer; altering or relaxing one or more of the modeling assumptions could change calculated thicknesses by several kilometers.

The slab velocities required by the observed travel times are very high, around 8.6 km/s at depths of 100 to 150 km. In fact, there is evidence, particularly for stations ETE and CHI that the slab velocities should be even higher than those we have used in our modeling.

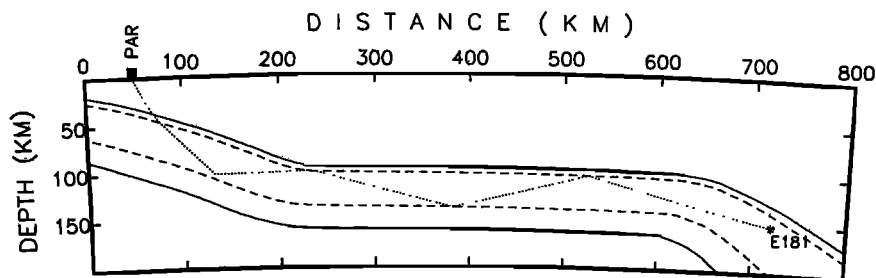


Figure 10. Ray path to station PAR from E181. For this geometry a festooning ray with four reflections is required, as the station is in shadow for both direct *P* and a doubly reflected festooning ray. The projection is through the station and along azimuth 17° .

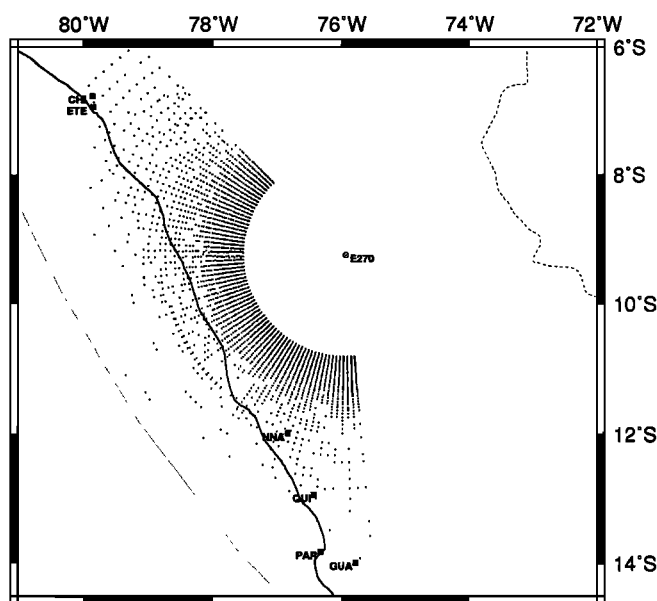


Figure 11. Map of surface intersections (small dots) of direct rays for event E270 traced through the slab model in equal increments of azimuth and takeoff angle. Note that stations PAR and GUA are in a shadow zone for direct rays.

Similarly large seismic velocity contrasts (4–12%) between slab and surrounding mantle have been reported in numerous studies of reflections and conversions at slab boundaries (see *Helfrich et al.* [1989] and *Helfrich and Stein* [1993] for a comprehensive summary). Travel time measurements of high slab velocities have been reported by *Gubbins and Snieder* [1991] for the Kermadec-Tonga subduction zone north of New Zealand, although the high velocities there were attributed to eclogitic oceanic crust at depths substantially greater than 100–150 km. On the other hand, results of velocity inversions from microseismicity in the Wellington region of New Zealand by *Robinson* [1986] indicate velocities in excess of 8.6 km/s, with those velocities in the cold mantle interior of the subducting plate.

Our results, along with the other seismic results cited above, appear to be inconsistent with recent studies of the thermal structure in subduction zones and the mineralogy of slabs [e.g., *Helfrich*, 1990; *Helfrich and Stein*, 1993] which suggest that thermal structure of the slab and differences in bulk composition between slab and surrounding mantle should make only minor con-

tributions to observed velocity contrasts. *Helfrich and Stein* [1993] propose that the different depths of phase transformations in the cold slab relative to hotter surrounding mantle can be major contributing factors to observed velocity contrasts, but these effects are confined primarily to depths greater than 200 km. There are no known phase transformations at depths of 100 to 150 km that would produce the very high velocity contrasts we observe.

It is known that laminated structures subject to shear stresses can acquire anisotropic properties [e.g., *Babuska and Cara*, 1991]. Because the subducting slab undergoes stress normal to the trench, anisotropy may develop, with the direction of fast polarization aligned parallel to the maximum stress direction. Recent studies [*Kaneshima and Silver*, 1992; *Russo and Silver*, 1994] of shear wave mantle anisotropy beneath central Peru found that while there is a fast polarization direction for *S* waves parallel to the trench, the anisotropy seems to reside primarily in the mantle beneath the slab. Shear wave splitting above the slab is only about 0.1 to 0.2 s, not enough to affect our results significantly. Moreover, the ray paths studied here are distributed over a wide range of azimuths relative to the direction of convergence, and no systematic effect is observed. From this, we conclude that anisotropy cannot be the cause of the abnormally high velocities we observe in the subducting Nazca plate beneath northern-central Peru.

If thermal effects alone are responsible for high seismic velocities in the slab, the temperatures would have to be low, around 400°C. This temperature is significantly lower than the approximately 500°C predicted by thermal models for the coldest 30 or 35 km of the slab interior (see discussion under Plate Structure above). The temperature of the slab interior for a given seismic velocity may be calculated from laboratory measurements of velocity. Consider oceanic lithospheric mantle of harzburgite comprised of 75% olivine, 20% orthopyroxene, and 5% garnet. We use the following values for *P* wave velocities and their *P* – *T* partial derivatives from *Christensen* [1982]:

1. Olivine: $V_P = 8.42$ km/s at room *P*, *T*; $\partial V_P / \partial P = 10.2$ km/s/mbar; $\partial V_P / \partial T = -4.86 \times 10^{-4}$ km/s/°C;
2. Orthopyroxene: $V_P = 7.78$ km/s at room *P*, *T*; $\partial V_P / \partial P = 20.6$ km/s/mbar; $\partial V_P / \partial T = -9.08$ km/s/°C;
3. Garnet (pyrope): $V_P = 8.53$ km/s at room *P*, *T*; $\partial V_P / \partial P = 7.84$ km/s/mbar; $\partial V_P / \partial T = -3.93 \times 10^{-4}$ km/s/°C.

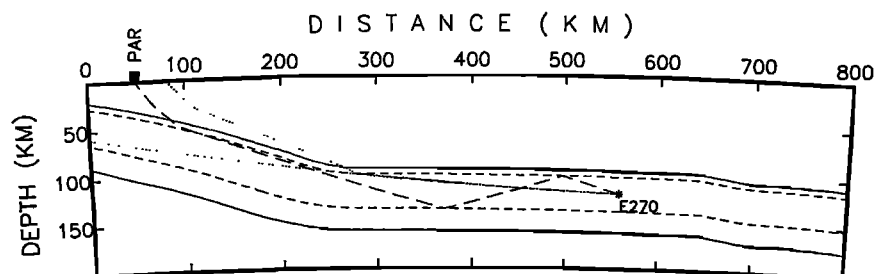


Figure 12. Ray paths to station PAR from E270. Station is in shadow for direct arrivals (dotted lines), but not for the double-bounce festooning ray (long dashes).

Thus, for $P = 40$ kbar (depth around 120 km) and $T = 400^\circ\text{C}$, the calculated P wave velocity for harzburgite would be 8.56 km/s. At 500°C the velocity would decrease to about 8.5 km/s. If T is reduced to 350°C , velocity increases only to 8.59 km/s, still at the low end of what is required to explain the observed travel times through the slab in central Peru. Relatively greater abundances of olivine or garnet will result in a slight increase in velocity at all temperatures, but the increase would not be sufficient to compensate for the negative thermal effect on velocities for temperatures significantly above 400°C in the interior of the slab.

Acknowledgments. This study was supported by NSF grants EAR-8720842, EAR-8720843, EAR-9018848, and EAR-901985 plus a one-year Carnegie predoctoral fellowship (for E. O.N.). Map plots were done using GMT (Wessel and Smith, 1991).

References

- Ahrens, T. J., and G. Schubert, Gabbro-eclogite reaction rate and its geophysical significance, *Rev. Geophys.*, **13**, 383–400, 1975.
- Babuska, V., and M. Cara, *Seismic Anisotropy in the Earth*, Kluwer Academic, Norwell, Mass., 1991.
- Barazangi, M., and B. Isacks, Spatial distribution of earthquakes and subduction of the Nazca plate beneath South America, *Geology*, **4**, 686–692, 1976.
- Boyd, T., J. A. Snoke, I. S. Sacks, and A. Rodriguez, High resolution determination of the Benioff zone geometry beneath southern Peru, *Bull. Seismol. Soc. Am.*, **74**, 557–566, 1984.
- Cahill, T., and B. L. Isacks, Seismicity and shape of the subducted Nazca plate, *J. Geophys. Res.*, **97**, 17,503–17,529, 1992.
- Chapman, D. S., and H. N. Pollack, Regional geotherms and lithospheric thickness, *Geology*, **5**, 265–268, 1977.
- Červený, V., L. Klimes, and I. Psencik, Complete seismic ray tracing in three-dimensional structures, in *Seismological Algorithms – Computational Methods and Computer Programs*, pp. 89–167, Academic, San Diego, Calif., 1988.
- Christensen, N. I., Seismic velocities, in *Handbook of Physical Properties of Rocks*, Vol. 2, edited by R. S. Carmichael, pp. 1–228, CRC Press, Inc., Boca Raton, Florida, 1982.
- Fukao, Y., S. Hori, and M. Ukawa, A seismological constraint on the depth of basalt-eclogite transition in a subducting oceanic crust, *Nature*, **303**, 413–415, 1983.
- Gubbins, D., and R. Snieder, Dispersion of P waves in subducted lithosphere: Evidence for an eclogite layer, *J. Geophys. Res.*, **96**, 6321–6333, 1991.
- Hasegawa, A., and I. S. Sacks, Subduction of Nazca plate beneath Peru as determined by seismic observations, *J. Geophys. Res.*, **86**, 4971–4980, 1981.
- Helfrich, G. R., Study of the structure of the slab-mantle interface using reflected and converted waves, Ph.D. dissertation, Dep. of Geol., Northwestern Univ., Evanston, Ill., 1990.
- Helfrich, G. R., S. Stein, and B. J. Wood, Subduction zone thermal structure and mineralogy and their relationship to seismic wave reflections and conversions at the slab/mantle interface, *J. Geophys. Res.*, **94**, 753–763, 1989.
- Helfrich, G. R., and S. Stein, Study of the structure of the slab-mantle interface using reflected and converted seismic waves, *Geophys. J. Int.*, **115**, 14–40, 1993.
- Henry, S. G., Terrestrial heat flow overlying the Andean subduction zone, Ph.D. dissertation, Univ. of Mich., Ann Arbor, 1981.
- Henry, S. G., and H. N. Pollack, Terrestrial heat flow above the Andean subduction zone in Bolivia and Peru, *J. Geophys. Res.*, **93**, 15,153–15,162, 1988.
- Jacob, K. H., Three dimensional seismic ray tracing in a laterally heterogeneous spherical earth, *J. Geophys. Res.*, **75**, 6675–6689, 1970.
- James, D. E., Andean crustal and upper mantle structure, *J. Geophys. Res.*, **76**, 3246–3271, 1971.
- James, D. E., and J. A. Snoke, Structure and tectonics in the region of flat subduction beneath central Peru, Part I, Crust and uppermost mantle, *J. Geophys. Res.*, in press, 1994.
- Jordan, T. E., B. L. Isacks, R. W. Allmendinger, J. A. Brewer, V. A. Ramos, and C. L. Ando, Andean tectonics related to geometry of subducted Nazca plate, *Geol. Soc. Am. Bull.*, **94**, 341–361, 1983.
- Julian, B. R., Raytracing on arbitrarily heterogeneous medium, Tech. Rep. 1970–45, Lincoln Lab., Mass. Inst. of Technology, Cambridge, 1970.
- Julian, B. R., and D. Gubbins, Three dimensional seismic raytracing, *J. Geophys.*, **43**, 95–114, 1977.
- Kaneshima, S., and P. G. Silver, A search for source side mantle anisotropy, *Geophys. Res. Lett.*, **19**, 1049–1053, 1992.
- Kennett, B. L. N., and E. R. Engdahl, Travel times for global earthquake location and phase identification, *Geophys. J. Int.*, **105**, 429–465, 1991.
- Lahr, J. C., HYPOELLIPSE/Version 2.0: A computer program for determining local earthquake hypocentral parameters, magnitude, and first motion pattern, *U.S. Geol. Surv. Open File Rep.*, **89–116**, 1992.
- Matsuzawa, T., N. Umino, A. Hasegawa, and A. Takagi, Upper mantle velocity structure estimated from PS-converted wave beneath the north-eastern Japan Arc, *Geophys. J. R. Astron. Soc.*, **86**, 767–787, 1986.
- Matsuzawa, T., N. Umino, A. Hasegawa, and A. Takagi, Estimation of thickness of a low-velocity layer at the surface of the descending oceanic plate beneath the northeastern Japan arc by using synthesized PS-wave, *Tohoku Geophys. J.*, **31**, 19–28, 1987.
- McNutt, M. K., Lithospheric flexure and thermal anomalies, *J. Geophys. Res.*, **89**, 11,180–11,194, 1984.
- Noble, D., and E. McKee, Spatial distribution of earthquakes and subduction of the Nazca plate beneath South America: A comment, *Geology*, **5**, 576–577, 1977.
- Noble, D., E. McKee, E. Farrar and U. Peterson, Episodic Cenozoic volcanism and tectonism in the Andes of Peru, *Earth Planet. Sci. Lett.*, **21**, 213–220, 1974.
- Robinson, R., Seismicity, structure, and tectonics of the Wellington region, New Zealand, *Geophys. J. R. Astron. Soc.*, **87**, 379–409, 1986.
- Russo, R. M., and P. G. Silver, Trench-parallel flow beneath the Nazca plate from seismic anisotropy, *Science*, **263**, 1105–1111, 1994.
- Sacks, I. S., The subduction of young lithosphere, *J. Geophys. Res.*, **88**, 3355–3366, 1983.
- Sacks, I. S., and H. Okada, A comparison of the anelasticity structure beneath western South America and Japan, *Phys. Earth Planet. Inter.*, **9**, 211–219, 1974.
- Schneider, J. F., and I. S. Sacks, Stress in the contorted Nazca plate beneath southern Peru from local earthquakes, *J. Geophys. Res.*, **92**, 13,887–13,902, 1987.
- Stauder, W., Subduction of the Nazca plate under Peru as evidenced by focal mechanisms and by seismicity, *J. Geophys. Res.*, **80**, 1053–1064, 1975.

- Vidale, J., Finite-difference calculation of travel times in 3-D, *Geophysics*, 55, 521–526, 1990.
- Watts, A. B., J. H. Bodine, and M. S. Steckler, Observations of flexure and the state of stress in the oceanic lithosphere, *J. Geophys. Res.*, 85, 1391–1398, 1980.
- Wessel, P., and W. H. F. Smith, Free software helps map and display data, *Eos Trans. AGU*, 72, 441, 445–446, 1991.
- Wiggins, R., A note on interpolating digitized curves, *Bull. Seismol. Soc. Am.*, 66, 2077–2081, 1976.
- E. O. Norabuena, Instituto Geofísico del Perú, Apartado 3747, Lima 100, Perú.
- J. A. Snoke, Virginia Tech Seismological Observatory, Department of Geological Sciences, Virginia Polytechnic Institute and State University, Blacksburg, VA 24061-0420.
- D. E. James, Department of Terrestrial Magnetism, Carnegie Institution of Washington, 5241 Broad Branch Road, N.W., Washington, DC 20015.

(Received May 6, 1993; revised December 3, 1993; accepted January 10, 1994.)